Development of a Piezoelectric Micromachined Ultrasound Transducer using Microfabrication Technology for in Vitro Neuromodulation

Ryo Furukawa[a] and Takashi Tateno[b]

*Bioengineering and Bioinformatics, Graduate School of Information Science and Technology, Hokkaido University,
Kita 14, Nishi 9, Kita-ku, Sapporo, Hokkaido 060-0814, Japan*

Keywords: Numerical Calculations, Microfabrication, Neuromodulation, Piezoelectric Micromachined Ultrasound Transducer, Ultrasound Brain Stimulation.

Abstract: Ultrasound neuromodulation, in which local and deep areas of the brain are stimulated, is promising for clinical applications. However, the mechanisms of action underlying the stimulation are still unknown. To elucidate the induction mechanisms, in vitro experiments are useful because they allow the extracellular conditions to be easily controlled. In this study, we developed a piezoelectric micromachined ultrasound transducer (PMUT) to modulate the activity of brain slices at the micrometer scale. To examine the relationship between the transducer size and the resonant frequency of the voltage-driven oscillations, we modeled the multi-layered structure and performed numerical calculations. A simple mathematical expression to estimate the size of the PMUT was obtained. We also designed and fabricated a PMUT with identical circular diaphragms with 580-μm radius. In addition, recording microelectrodes were fabricated into the PMUTs to monitor the transducer-driven neural activity. To characterize the PMUT properties, including the intensity and resonant frequency, we measured the pressure oscillations of the transducer driven by the applied sinusoidal voltage. Finally, we discuss the possibility of using our PMUT to stimulate brain slices in future applications.

1 INTRODUCTION

Neuromodulation techniques have been studied as promising tools for the treatment of brain diseases (Bewernick et al., 2010). Because the intensity of electromagnetic waves attenuates with increasing distance, noninvasively inducing transcranial neural responses in deep brain regions is difficult using conventional methods, such as transcranial direct current and magnetic stimulation methods (Wagner et al., 2007). Overcoming this limitation, transcranial ultrasound stimulation has recently drawn attention owing to its low- or non-invasiveness and higher spatial resolution (Tufail et al., 2010).

Neural impulses have historically been considered to be electrical signals; the suprathreshold depolarization of neural membranes was also influenced by mechanical mechanisms. Thus, describing a neural impulse via a mechanical pathway could support a physical basis for ultrasound-driven neuromodulation. However, its underlying mechanisms at the cellular level are still unknown. A reason for this is the lack of an in vitro method for stimulating local circuits in the brain with this technology at high spatial resolution. In addition, indirect neural activity through polysynaptic pathways could affect the neuromodulation, which further complicates the investigation of the mechanism of action (Sato et al., 2018). conventional ultrasound transducers are of limited use for brain stimulation because they are too large (>10 mm) to locally stimulate neurons on a spatial scale of tens to hundreds of micrometers.

Microelectromechanical system (MEMS) technology has recently been used to produce a transducer for ultrasound brain stimulation. For example, Kim et al. developed a capacitive

micromachined ultrasound transducer (CMUT) and conducted an in vivo experiment to stimulate the brain of a freely moving mouse (Kim et al., 2019) ; their CMUT stimulated the brain regions on a scale of 2.8 mm. In addition, Lee et al. developed a piezoelectric micromachined ultrasound transducer (PMUT) and demonstrated its effectiveness for elucidating the cellular mechanisms of neuromodulation in cultured neural networks in vitro (Lee et al., 2019). However, in their experiments with cultured brain cells, because neurons in the neural tissue were isolated and rewired in cultured networks, the original neural networks were rebuilt in networks with a random connection.

For a given energy input, PMUTs are more effective than CMUTs in driving micrometer-sized ultrasound transducers (Manwar et al., 2020). Therefore, we used PMUTs in this study. We examined how the device structure influences the resonant frequency and the intensity of the generated ultrasound. In addition, we propose that an in vitro experimental system is useful for examining the cellular mechanisms of ultrasound neuromodulation because it allows the extracellular conditions of the targeted neurons to be easily controlled.

We first examined the relationships among the multi-layered PMUT structure, the size of the diaphragms in the transducer, and the resonant frequency of the transducer. Each of the diaphragms was designed to resonate at 500 kHz for neural stimulation. A physical model of the PMUT was constructed. The relationships among the PMUT properties were analytically calculated using this model and the physical parameters of the PMUT
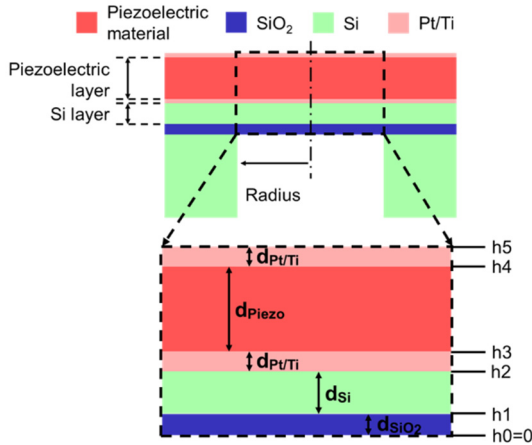

Figure 1: Cross-section of the PMUT, which consisted of piezoelecctric material, Si, SiO₂, and Pt/Ti layers. The expanded view of the top pannel (dashed square) is shown in the bottom panel. The layer thicknesses are indicated by arrows, which are considered in Eqs (5) and (7).

materials. In addition, the result of the analytical calculation was compared with that of numerical simulations using multiphysics software. We then designed a PMUT and circular diaphragms as microelectrodes to simultaneously record the neural activity in a brain slice under ultrasound stimulation. Because the ultrasound-driven response is strongly dependent on the background activity of neural circuits, we consider that PMUT devices equipped with recording electrodes are more appropriate than conventional methods without recording functions for neural stimulation. To characterize the PMUT properties, including the intensity and resonant frequency, we measured the pressure oscillations of the transducer driven by the applied sinusoidal voltage. Finally, we examine whether our PMUT has the potential to effectively stimulate local networks in brain slices in future studies.

2 METHODS

To locally stimulate brain slices, we aimed to develop a PMUT that satisfies three numerical conditions: (i) a resonant frequency of the diaphragm of 500 kHz, (ii) an ultrasound intensity for stimulation greater than 0.5 W/cm² , and (iii) a diaphragm radius smaller than 0.6 mm (Lee et al., 2019).

2.1 The PMUT Model and Numerical Calculations

Our PMUT consisted of the following five components: a piezoelectric film, a silicon (Si) layer, a SiO₂ membrane, top and bottom Pt/Ti electrodes, and a Si supporting layer (Fig. 1). To convert electric (voltage) signals into ultrasound pressures, a thin film of a piezoelectric material was used as the transducer. To achieve a thin diaphragm as a vibrating plate, circular drains were designed from the back side of the supporting Si substrate (Fig. 1, top); for the experiments, the PMUT device was inverted.

The simple diaphragm model of the PMUT is described below. A diaphragm was first modeled as a single-layered circular plate with radius r_0, before a multi-layered case was considered. The position on the plate was represented by a two-dimensional polar coordinate (r, θ) with the plate center defined as $r = 0$. If a uniform radial tension T is applied to the plate, the deflection $w(r, \theta)$ of the plate from the resting state can be expressed as (Wah, 1962):

$$D\nabla^4 w - T\nabla^2 w + \rho \frac{\partial^2 w}{\partial t^2} = 0 , \qquad (1)$$

where t is the time, ∇^2 and ∇^4 are the Laplace operator and the biharmonic operator, respectively. Here, ρ is the density per unit area of the plate, and D is the flexural rigidity of the plate, which can be written as:

$$D = \frac{Eh^3}{12(1-\nu^2)}, \qquad (2)$$

where E is Young's modulus, h is the thickness, and ν is the Poisson ratio (Wah, 1962).

The actual circular diaphragm consists of multiple layers, as shown in Fig. 1. Thus, using each thickness, d_i, of the layers and the corresponding volume density, ρ_i, from the bottom to the top ($i = 1, \cdots, 5$), the total mass per plate area, ρ_m, for the multiple layers can be described as:

$$\rho_\mathrm{m} = \sum_i \rho_i d_i . \qquad (3)$$

Similarly, the height, h_n, of the n-th layer ($n = 1, \cdots, 5$) is defined as:

$$h_n = \sum_{i=1}^{n} d_i . \qquad (4)$$

Furthermore, according to Ref. (Muralt et al., 2005), the stress center z_s is defined as:

$$z_\mathrm{s} = \frac{1}{2}\left(\frac{h_n^2 - h_{n-1}^2}{se(n)}\right)\Big/\left(\frac{d_n}{se(n)}\right), \qquad (5)$$

where $se(n)$ indicates the relevant compliance of the n-th layer. $se(n)$ can be described as (Muralt et al., 2005):

$$se(n) = s_{11}^{(n)}(1 - v(n)^2) , \qquad (6)$$

where $s_{11}^{(n)}$ denotes the elastic compliance term of each layer, and the subscript represents the usual tensor compliance notation. For the multi-layered plate, the flexural rigidity, D_m, of the diaphragm can be described as (Muralt et al., 2005):

$$D_\mathrm{m} = \frac{1}{3}\sum_n \frac{(h_n - z_\mathrm{s})^3 - (h_{n-1} - z_\mathrm{s})^3}{s_{11}^{(n)}(1 - v(n)^2)} . \qquad (7)$$

Two extreme types of boundary conditions for the vibrating plate governed by Eq. (1) were considered: (i) a clamped condition (CC) and (ii) a simply supported condition (SSC). On the boundary of the plate ($r = r_0$), the CC is described as:

$$w = 0 , \qquad (8a)$$

$$\frac{\partial w}{\partial r} = 0 . \qquad (8b)$$

The SSC is described as:

$$w = 0 , \qquad (9a)$$

$$\frac{\partial^2 w}{\partial r^2} + \nu\left(\frac{1}{r}\frac{\partial w}{\partial r} + \frac{1}{r^2}\frac{\partial^2 w}{\partial \theta^2}\right) = 0 , \qquad (9b)$$

where θ represents an angular variable of the polar coordinates. In this manuscript, both ideal boundary conditions were applied in the numerical calculation. By solving Eq. (1) analytically with the CC or SSC, the relationship among the plate radius, r_0, resonant frequency f_r, and other plate parameters can be described as:

$$r_0^2 = \frac{\alpha\beta}{2\pi f_\mathrm{r}}\sqrt{\frac{D_\mathrm{m}}{\rho_\mathrm{m}}}, \qquad (10)$$

where α and β are constants that depend on the boundary conditions (Wah, 1962): $(\alpha, \beta) = (2.84, 6.16)$ for the CC and $(\alpha, \beta) = (2.31, 3.71)$ for the SSC. We note that actual vibration of such plates corresponds to a boundary condition between these two extreme boundary conditions.

To characterize the relationships among the radius and thickness of a diaphragm, and the resonant frequency, we performed the numerical calculation of the multi-layered circular plate. First, we calculated the forced oscillation properties for the physical model of the plate with five layers: top Pt/Ti electrode, piezoelectric material, bottom Pt/Ti electrode, Si, and SiO$_2$ layers (Fig. 1, bottom). The thicknesses of these layers were assumed to be 0.10, d_piezo, 0.10, d_Si, and 1.0 μm, respectively (Table 1). For convenience, the two Ti/Pt-electrode layers were simplified as single Pt layers. The thicknesses of the Pt/Ti electrode and SiO$_2$ layers were fixed because they were much thinner than the other two materials. The goal of the numerical calculation was to determine the appropriate radius of the diaphragm, and thicknesses of the piezoelectric material and Si layers when the diaphragm resonates in response to a 500-kHz sinusoidal input.

Table 1: Material parameters used in the numerical calculation.

Material	Thickness in μm	Young's modulus in GPa	Density in kg/m³	Poisson's ratio
PZT	d_{piezo}	63	7500	0.34
Si	d_{Si}	170	2329	0.28
SiO₂	1.0	70	2200	0.17
Pt	0.1	168	2145	0.38

To confirm the results from the numerical calculation, we also performed a numerical simulation, using general-purpose physics simulation software (COMSOL Multiphysics, Ver. 5.5, COMSOLAB, Sweden) on a supercomputer system (PRIMERGY CX400/CX2550, FUJITSU, Japan) at the Hokkaido University Computer Center. Using the finite-element method (FEM) in this simulation software, we calculated the resonant frequency and determined the sizes of the PMUT. We modeled the five-layered plate with d_{piezo} and d_{Si} and compared the results with those of the calculation. Before the simulation, we determined the mesh size, which split the modeling domain into a discrete number of elements; the mesh size ranged from 12.6 to 70.0 μm. In the simulation, the resonant frequencies were calculated using frequency-domain analysis. We used lead zirconate titanate (PZT) as the piezoelectric material in the simulation because this was used in our microfabrication process, which is described below. The thicknesses of the PZT and Si layers ranged from 25 to 250 μm and 7 to 35 μm, respectively. All parameters of the four materials used in the simulation are listed in Table 1.

To obtain simple mathematical relationships among r_0, d_{piezo}, and d_{Si} under a 500-kHz resonant-frequency condition with the first resonant mode (0, 1) (Hong et al., 2006), we collected 50 data points of the triplet parameters (r_0, d_{piezo}, d_{Si}) from the FEM simulation. Low-order polynomial functions of the three parameters were fitted to the data points using a least-square approximation. For the five-layered model, optimal functions were determined on the basis of minimizing the square errors between the fitted functions and the data points.

2.2 PMUT Design and Microfabrication Processes

To stimulate a brain slice with high-spatial resolution, the PMUT was designed with an array of four diaphragms (Fig. 2). Microelectrodes (200 × 200 μm²) were also designed on the substate to simultaneously record the electrical activity of the brain slice. The sizes of the diaphragms were determined from the results of the numerical simulation to optimally resonate the plates at 500 kHz.

Our microfabrication process was based on MEMS technology and the initial substrate was a silicon-on-insulator (SOI) wafer consisting of three layers: a device layer (Si), an insulating membrane (SiO₂), and a handle layer (Si). Briefly, our microfabrication process is described as follows:

(1) We used an SOI substrate with a Si handle layer (500 μm), an insulating membrane (1 μm), and a Si device layer (10 μm). We deposited 1-μm-thick SiO₂ on the bottom side (Fig. 3A).

(2) As the electrode material, a layer comprising a 100-nm-thick Pt coating and 10-nm-thick Ti coating was deposed on the substrate using a sputtering system (RSC-3ERD, Riken-sha Co., Japan). Subsequently, the recording electrodes and their wires were patterned on the bottom side by photolithography (Fig. 3B).

(3) We formed the recording electrodes and their wires on the substrate using an inductively coupled plasma reactive ion etching (ICP-RIE) system (RIE-101HU, SUMCO Co., Japan). Subsequently, the protective film for the wires was formed on the bottom side (Fig. 3C).

(4) An epoxy resin (bond E205) was applied on the bottom side by the sputtering system. Thereafter, the PZT film was attached on the top of the substrate (Fig. 3C).
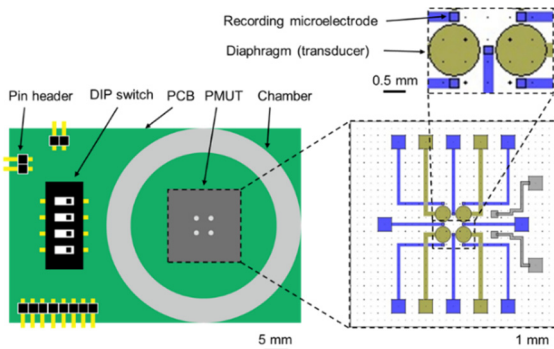

Figure 2: Design of a printed circuit board (left) and the PMUT (lower right) with an array of four diaphragms and eight recording electrodes (upper right).
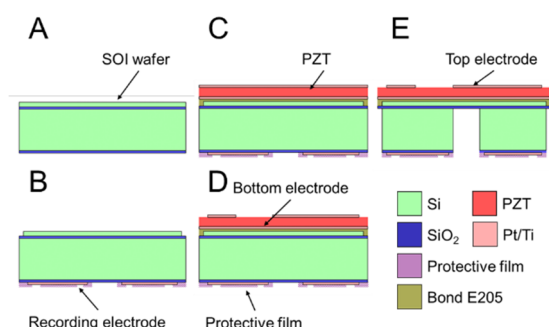
Figure 3: Microfabrication processes used to construct our PMUT. The different colors represent the different materials (Si, PZT, SiO$_2$, Pt/Ti, protective film, and epoxy resin E205). The thickness of each material in the figure does not reflect its actual size.

(5) The top electrodes of the PZT and their wires to drive the diaphragms were patterned and formed using the ICP-RIE system (Fig. 3D).

(6) As the final step to create the diaphragm shape, the Si handle layer was removed from the back side using a Deep-RIE instrument (MUC-21 ASE-SRE, SPP Technologies Co., Japan). The last remaining surface-resist layer was removed using acetone and isopropyl alcohol (Fig. 3E).

2.3 Measurement of PMUT Properties

To characterize the properties of the fabricated PMUTs, we measured the resonant frequencies of the diaphragms. In the present study, four PMUT devices were used in the measurement. Initially, a cylindrical acrylic chamber with an internal diameter of 30 mm was attached to the substrate on a custom-made printed circuit board (Fig. 2, left). Subsequently, individual diaphragms in the PMUT were driven by a sinusoidal signal with a voltage amplitude of 10 V, which was generated by a multifunction generator (WF1947, NF Electronic Instruments, Japan) through a high-speed bipolar amplifier (HSA4014, NF Electronic Instruments) with a 10-times voltage gain. The frequencies ranged from 250 to 800 kHz. In the measurement, the chamber, including the PMUT, was filled with water. The generated acoustic pressure just above the diaphragm in the chamber was measured with a calibrated needle hydrophone (HY05N, Toray Engineering Co., Japan); the distance between the diaphragm and the hydrophone was approximately 1 mm. The data obtained from the hydrophone was recorded by an oscilloscope (DSOX1102G, Keysight Technologies, USA) with a digital data-acquisition system. In the measurement, the measured resonant

frequency was obtained as the frequency at which the maximum peak response was in the frequency range (i.e., 250–800 Hz) of the applied voltage signals. The error rate (%) was calculated as $100 \times |fr - 500| / 500$ (fr in kHz). In addition, as an index of ultrasound intensity, we used the time-integral intensity (spatial peak pulse average, I_{sppa}) (Fomenko et al., 2018), which is defined as the time-averaged power of acoustic pressure, normalized by the density of the fluid medium (i.e., water) and the velocity inside the medium, during a certain period.

3 RESULTS

3.1 Expression of the Three Parameters

Figure 4 shows the relationships among the size parameters (r_0, d_{PZT}, and d_{Si}) of the diaphragm under a resonant frequency of 500 kHz. In both plots, the
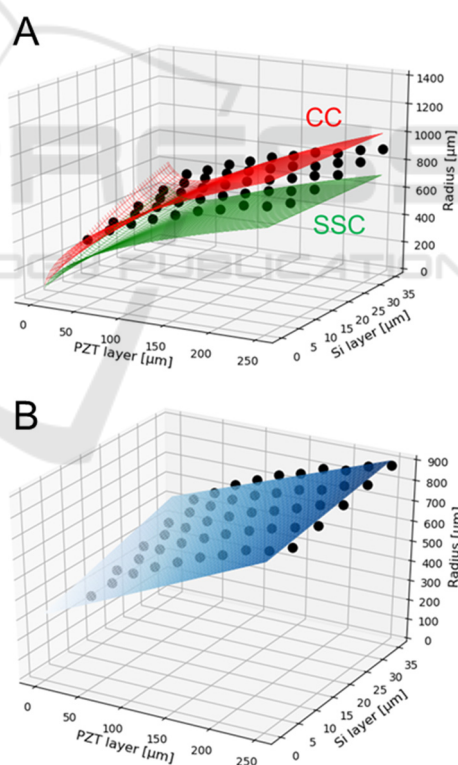

Figure 4: Relationships among the three size parameters (r_0, d_{PZT}, d_{Si}). In both plots, the black dots represent the data points from the FEM simulations of the five-layered physical model. (A) The red and green curves represent the relationships obtained Eq. (10) under the CC and SSC, respectively. (B) The blue curve represents the relationship described by Eq. (11).

data points indicated by dots were obtained from the FEM simulation of the five-layered plate model; these data points are identical in the two plots. The simulation result indicates that r_0 monotonically increases as the thickness of the PZT layer or the Si layer increases. Moreover, Eq. (11) was determined by applying the least-squares method to the FEM data (Fig. 4B):

$$r_0(d_{\text{PZT}}, d_{\text{Si}}) = 315 + 5.72 d_{\text{Si}} + 1.98 d_{\text{PZT}} \\ -11.9 \times 10^{-3} d_{\text{PZT}} d_{\text{Si}} \quad (11)$$

The relationship for the five-layered plate was approximately described as four terms, including a second-order polynomial of $d_{\text{PZT}} \times d_{\text{Si}}$ ($R^2 = 0.975$). The result (Fig. 4A) shows that the red curve of the three size parameters for the model under the CC overestimates the plate radius compared with the FEM simulation (black dots). By contrast, the green curve for the five-layered model under the SSC underestimates the plate radius. These numerical results suggest that the actual vibration of such plates corresponds to a boundary condition between the CC and SSC. In addition, we determined d_{PZT} and d_{Si} to be 100 and 10 μm, respectively, and r_0 to be 580 μm based on the numerical calculations (Fig. 2).

3.2 Microfabrication of the Diaphragm

We successfully microfabricated the PMUT device with four diaphragms and eight microelectrodes (Fig. 5). The packaged and enlarged PMUTs are illustrated in Fig. 5A and 5B, respectively.
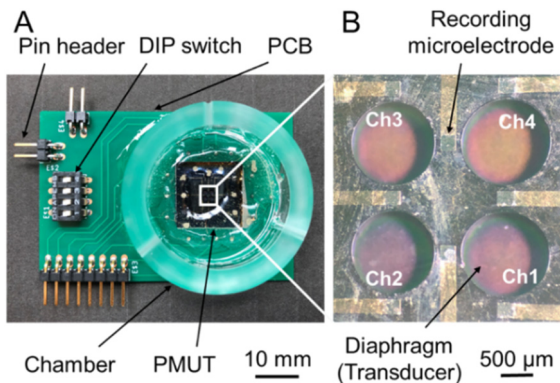

Figure 5: Images of the microfabricated PMUT. (A) The packaged substrate with the PMUT device. (B) Front side of the PMUT with four diaphragms (channels, Chs) and eight electrodes (corresponding to the bottom side of the schematic illustration in Fig. 3E).

3.3 Response Characteristics of the Fabricated PMUT

To characterize the response of the fabricated PMUT, we measured the acoustic pressure of individual diaphragms when the PMUT was driven by sinusoidal voltage signals (AC amplitude, 10–50 V). A typical example of the frequency response for four diaphragms (channels 1 to 4) is illustrated in Fig. 6A for an AC amplitude of 10 V. In the pressure measurement, the maximum of acoustic pressure was 27.4 kPa in channel 3 at 680 kHz. In channels 1, 3, and 4, resonance phenomena were seen at specific frequencies, while the resonant acoustic pressure was smaller in channel 2 (10.4 kPa) than ones in other channels. In addition, although each of the resonant
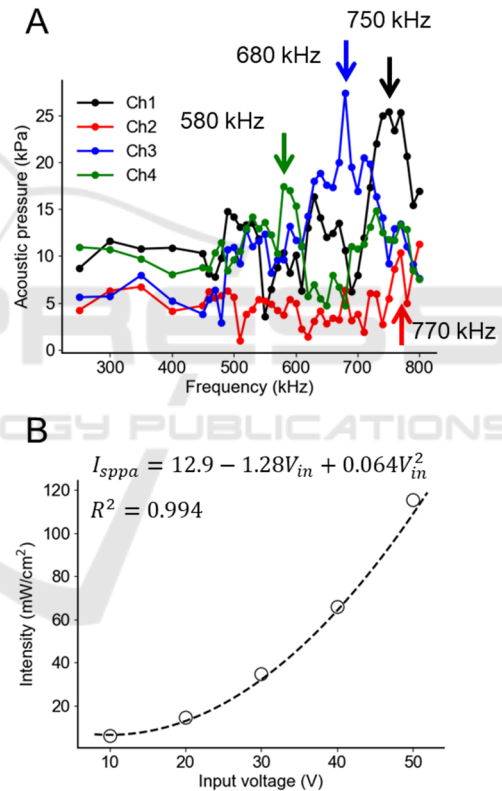

Figure 6: Measured acoustic characteristics of the fabricated PMUT and an intnsity estimation from the data points. (A) Measured acoustic pressure as a function of frequency for a sinusoidal voltage input. These frequency response characteristics were obtained by applying a 10-V signal at different frequencies. The channel numbers correspond to those shown in Fig. 5B. The resonant frequencies are indicated by the arrows in each channles. (B) Resonant acoustic intensities for different input voltages. The dashed line represents the relationship between input voltages and resultant intensities as a quadratic function described by Eq. (12).

frequencies was different from the targeted frequency (i.e., 500 kHz), the error rate of the four diaphragms was $39 \pm 15\%$ for the PMUT device (Fig. 6A). Overall, the error rate of the seven diaphragms out of three examined PMUT devices was $42\pm12\%$.

Moreover, when the input voltage amplitude was increased, the response intensity at the resonant frequency monotonically was increased (Fig. 6B). The relationship between the response intensity, I_{sppa} (in mW/cm^2), and input voltage amplitude, V_{in} (in V), was approximated by the following quadratic function ($R^2 = 0.994$):

$$I_{\mathrm{sppa}}(V_{\mathrm{in}}) = 12.9 - 1.28V_{\mathrm{in}} + 0.064V_{\mathrm{in}}^2 . \quad (12)$$

Here, a standard linear regression method was used to minimize the mean square error between the data points and the quadratic function of V_{in} with three parameters. From Eq. (12), we can estimate that individual diaphragms of the PMUT could approximately generate 0.5 W/cm^2 integral intensity when a sinusoidal voltage signal of 100 V is applied, which satisfies our initial target intensity in this study.

4 DISCUSSION

In this study, we developed a MEMS-based PMUT to locally stimulate brain slices in vitro. We performed numerical simulations to examine the relationships between the diaphragm size and the resonant frequency of the voltage-driven oscillations. Modeling the multi-layered structure of the PMUT diaphragms and FEM simulations provided a simple mathematical expression to estimate the PMUT size. For the five-layered diaphragm, the curve describing the relationship among the three size parameters was positioned between those based on the analytical results (Eq. (12)) under the CC and SSC. Therefore, the analytical expression of Eq. (12) gives a rough estimate of the three size parameters and would be useful for selecting the size parameters in preliminary study stages. In addition, the data points obtained from the FEM simulation were approximated as a function of the low-order polynomials. The expression of the low-order polynomials provides a direct quantitative formula for a specific structural condition under the resonant frequency of 500 kHz. Thus, the result of the simple expression may be also useful for the design of PMUT devices because a frequency of 500 kHz is often selected for ultrasound brain stimulation.

On the basis of the numerical results, we designed and microfabricated a PMUT with four identical circular diaphragms with 580-μm radius and eight recording electrodes. To the best of our knowledge, this is the first time that recording electrodes have been fabricated in a PMUT, although we did not evaluate their electrical properties. Furthermore, to characterize the PMUT properties, including the intensity and resonant frequency, we measured the response of the transducer driven by a sinusoidal voltage input. Some diaphragms (e.g., channel 4) had a measured value (f_{r} = 580 kHz)) close to the target resonant frequency. We compared the difference between numerically predicted and measured resonant frequency with some previous reports. Then, our mean error rate 39% was relatively large compared with the previous studies (10-30%) (Cheng et al., 2019; Dangi et al., 2020; Lee et al., 2019; Lucia MS, 2017). In addition, among the four diaphragms, the variance of the resonance frequency was large (standard deviation = 74 kHz), and frequency-response characteristics were not identical. Although the reasons for the differences between the numerically predicted and measured values are not clear, we speculate that there was discrepancy between the fabricated and designed layer thicknesses of the diaphragms. To confirm this speculation in future work, we will take scanning electron microscope images of the PMUT cross-section to measure the layer thicknesses.

In addition, the input–output characteristic properties of the diaphragms imply that the intensities generated by the fabricated PMUT were similar to those predicted (> 0.5 W/cm^2), which is sufficient for the stimulation of brain slices in vitro. Our estimation requires feeding more than 100-V input into the device, how the electric artifacts affect the activity of neural tissue will be one of our future challenges.

Several recent review papers (Cardenas-rojas et al., 2021; Pasquinelli et al., 2019) summarized four potential mechanisms by which ultrasound signals could trigger action potentials: (i) the generation of capacitive currents as a result of membrane displacements, (ii) the activation of mechanosensitive channels, (iii) sonoporation in the lipid bilayer, and (iv) coupling with membrane waves along the axon. Effective ultrasonic neurostimulation may be possible by combining these mechanisms. Examining the mechanisms will be included in our future work.

MEMS processes. This work was supported by a Grant-in-Aid for Exploratory Research [grant number 18K19794] and a Grant-in-Aid for Scientific Research (B) [grant number 19H04178] (Japan).

REFERENCES

Bewernick, B. H., Hurlemann, R., Matusch, A., Kayser, S., Grubert, C., Hadrysiewicz, B., Axmacher, N., Lemke, M., Cooper-Mahkorn, D., Cohen, M. X., Brockmann, H., Lenartz, D., Sturm, V., & Schlaepfer, T. E. (2010). Nucleus Accumbens Deep Brain Stimulation Decreases Ratings of Depression and Anxiety in Treatment-Resistant Depression. *Biological Psychiatry*, *67*(2), 110–116. https://doi.org/10.1016/j.biopsych.2009.09.013

Cardenas-rojas, A., Pacheco-barrios, K., Giannoni-luza, S., Fregni, F., Rehabilitation, S., Hospital, M. G., Loyola, S. I. De, & Health, M. (2021). *HHS Public Access*. *20*(4), 401–412. https://doi.org/10.1080/14737175.2020.1738927.Non-invasive

Cheng, C. Y., Dangi, A., Ren, L., Tiwari, S., Benoit, R. R., Qiu, Y., Lay, H. S., Agrawal, S., Pratap, R., Kothapalli, S. R., Mallouk, T. E., Cochran, S., & Trolier-Mckinstry, S. (2019). Thin Film PZT-Based PMUT Arrays for Deterministic Particle Manipulation. *IEEE Transactions on Ultrasonics, Ferroelectrics, and Frequency Control*, *66*(10), 1605–1615. https://doi.org/10.1109/TUFFC.2019.2926211

Dangi, A., Cheng, C. Y., Agrawal, S., Tiwari, S., Datta, G. R., Benoit, R. R., Pratap, R., Trolier-Mckinstry, S., & Kothapalli, S. R. (2020). A Photoacoustic Imaging Device Using Piezoelectric Micromachined Ultrasound Transducers (PMUTs). *IEEE Transactions on Ultrasonics, Ferroelectrics, and Frequency Control*, *67*(4), 801–809. https://doi.org/10.1109/TUFFC.2019.2956463

Fomenko, A., Neudorfer, C., Dallapiazza, R. F., Kalia, S. K., & Lozano, A. M. (2018). Low-intensity ultrasound neuromodulation: An overview of mechanisms and emerging human applications. *Brain Stimulation*, *11*(6), 1209–1217. https://doi.org/10.1016/j.brs.2018.08.013

Hong, E., Trolier-McKinstry, S., Smith, R., Krishnaswamy, S. V., & Freidhoff, C. B. (2006). Vibration of micromachined circular piezoelectric diaphragms. *IEEE Transactions on Ultrasonics, Ferroelectrics, and Frequency Control*, *53*(4), 697–705. https://doi.org/10.1109/TUFFC.2006.1611029

Kim, H., Kim, S., Sim, N. S., Pasquinelli, C., Thielscher, A., Lee, J. H., & Lee, H. J. (2019). Miniature ultrasound ring array transducers for transcranial ultrasound neuromodulation of freely-moving small animals. *Brain Stimulation*, *12*(2), 251–255. https://doi.org/10.1016/j.brs.2018.11.007

Lee, J., Ko, K., Shin, H., Oh, S. J., Lee, C. J., Chou, N., Choi, N., Tack Oh, M., Chul Lee, B., Chan Jun, S., & Cho, I. J. (2019). A MEMS ultrasound stimulation system for modulation of neural circuits with high spatial resolution in vitro. *Microsystems and Nanoengineering*, *5*(1). https://doi.org/10.1038/s41378-019-0070-5

Lucia MS, H. K. and T. J. D. C. (2017). HHS Public Access. *Physiology & Behavior*, *176*(10), 139–148. https://doi.org/10.1109/ICSENS.2018.8589733.Evaluation

Manwar, R., Kratkiewicz, K., & Avanaki, K. (2020). Overview of ultrasound detection technologies for photoacoustic imaging. *Micromachines*, *11*(7), 1–24. https://doi.org/10.3390/mi11070692

Muralt, P., Ledermann, N., Paborowski, J., Barzegar, A., Gentil, S., Belgacem, B., Petitgrand, S., Bosseboeuf, A., & Setter, N. (2005). Piezoelectric micromachined ultrasonic transducers based on PZT thin films. *IEEE Transactions on Ultrasonics, Ferroelectrics, and Frequency Control*, *52*(12), 2276–2288. https://doi.org/10.1109/TUFFC.2005.1563270

Pasquinelli, C., Hanson, L. G., Siebner, H. R., Lee, H. J., & Thielscher, A. (2019). Safety of transcranial focused ultrasound stimulation: A systematic review of the state of knowledge from both human and animal studies. *Brain Stimulation*, *12*(6), 1367–1380. https://doi.org/10.1016/j.brs.2019.07.024

Sato, T., Shapiro, M. G., & Tsao, D. Y. (2018). Ultrasonic Neuromodulation Causes Widespread Cortical Activation via an Indirect Auditory Mechanism. *Neuron*, *98*(5), 1031-1041.e5. https://doi.org/10.1016/j.neuron.2018.05.009

Tufail, Y., Matyushov, A., Baldwin, N., Tauchmann, M. L., Georges, J., Yoshihiro, A., Tillery, S. I. H., & Tyler, W. J. (2010). Transcranial Pulsed Ultrasound Stimulates Intact Brain Circuits. *Neuron*, *66*(5), 681–694. https://doi.org/10.1016/j.neuron.2010.05.008

Wagner, T., Valero-Cabre, A., & Pascual-Leone, A. (2007). Noninvasive human brain stimulation. *Annual Review of Biomedical Engineering*, *9*, 527–565. https://doi.org/10.1146/annurev.bioeng.9.061206.133100

Wah, T. (1962). Vibration of Circular Plates. *The Journal of the Acoustical Society of America*, *34*(3), 275–281. https://doi.org/10.1121/1.1928110